Published in final edited form as:

Acad Radiol. 2016 December ; 23(12): 1545–1552. doi:10.1016/j.acra.2016.07.016.

Quantitative prediction of stone fragility from routine single and dual energy CT: proof of feasibility

Andrea Ferrero, PhD[1], **Juan C. Montoya, BS**[1], **Lisa E. Vaughan, MS**[2], **Alice E. Huang, BS**[1], **Ian O. McKeag**[1], **Felicity T. Enders, PhD**[2], **James C. Williams Jr, PhD**[3], and **Cynthia H. McCollough, PhD**[1,*]

[1]Department of Radiology, Mayo Clinic, Rochester, MN, 55905

[2]Department of Biomedical Statistics and Informatics, Mayo Clinic, Rochester, MN, 55905

[3]Department of Anatomy and Cell Biology, Indiana University School of Medicine, Indianapolis, IN, 46202-5120

Abstract

Rationale and Objectives—Previous studies have demonstrated a qualitative relationship between stone fragility and internal stone morphology. The goal of this study was to quantify morphological features from dual-energy CT images and assess their relationship to stone fragility.

Materials and Methods—Thirty-three calcified urinary stones were scanned with micro CT. Next, they were placed within torso-shaped water phantoms and scanned with the dual-energy CT stone composition protocol in routine use at our institution. Mixed low-and high-energy images were used to measure volume, surface roughness, and 12 metrics describing internal morphology for each stone. The ratios of low- to high-energy CT numbers were also measured. Subsequent to imaging, stone fragility was measured by disintegrating each stone in a controlled *ex vivo* experiment using an ultrasonic lithotripter and recording the time to comminution. A multivariable linear regression model was developed to predict time to comminution.

Results—The average stone volume was 300 mm^3 (range 134–674 mm^3). The average comminution time measured *ex vivo* was 32 s (range 7–115 s). Stone volume, dual-energy CT number ratio and surface roughness were found to have the best combined predictive ability to estimate comminution time (adjusted R^2= 0.58). The predictive ability of mixed dual-energy CT images, without use of the dual-energy CT number ratio, to estimate comminution time was slightly inferior, with an adjusted R^2 of 0.54.

Conclusion—Dual-energy CT number ratios, volume, and morphological metrics may provide a method for predicting stone fragility, as measured by time to comminution from ultrasonic lithotripsy.

[*]**Corresponding Author**, 200 First Street SW, Rochester, MN 55905, Phone: (507) 284-2511, Fax: (507) 266-3661, mccollough.cynthia@mayo.edu.

Keywords

Lithotripsy; Kidney Calculi; X-Ray Computed Tomography

Introduction

Symptomatic urinary stone disease affects approximately 900,000 persons in the United States each year, resulting in an estimated annual medical expenditure of over $1 billion in 2007 among Medicare beneficiaries alone (1, 2). The prevalence of kidney stones in the United States rose by 37% between 1976–1980 and 1988–1994 in both genders (3). Due to the effects of global warming, it has been predicted that there could be an increase of 1.6–2.2 million lifetime cases of urinary stones by 2050 in the United States alone, as kidney stones tend to form more frequently in states where dehydration is common (4).

Several surgical options are available for the 10–20% of symptomatic stone formers who fail to pass their stones spontaneously (5). Larger, harder kidney stones and those located in the lower pole of the kidney tend to be more easily fragmented and removed by percutaneous nephrolithotripsy (PCNL), a minimally invasive procedure whereby the stone is accessed through a small flank incision which allows direct visualization and intracorporeal ultrasonic lithotripsy for stone disruption and removal of fragments (6). Stone fragility, which we define as the time to comminution by a given surgical procedure, is affected by the extent of the stone burden (i.e., the size and number of stones) as well as its mineral composition (7).

Computed tomography (CT) is the recommended method for non-invasively imaging stones in the urinary tract as it can provide accurate sub-millimeter details of the size and location of stones anywhere along the urinary system (8, 9). However, differences in x-ray attenuation (i.e. CT numbers) from a single peak potential do not accurately discriminate between different stone types (10). Dual-energy CT, whereby attenuation properties of tissue are measured at two different peak x-ray energies to provide a measure of effective atomic number, has proven to be extremely effective at discriminating uric acid (UA) stones from non-uric acid (NUA) stones (11, 12) without increasing the radiation dose compared to single energy exams (10, 13); it is now the routine outpatient examination for symptomatic kidney stone patients at our institution. Limited success in further separating NUA stones (calcium oxalate, hydroxyapatite, cysteine and struvite) has also been reported (14, 15).

Among others, Williams *et al.* reported wide variability in stone fragility (i.e. ease of breakage) within groups of stones having the same mineral composition, suggesting that variation in stone structure could also play an important role (7). His group also investigated possible correlation between CT-visible structures and time to comminution by shock-wave lithotripsy (SWL) for a variety of stone types, including brushite (16), cystine (17) and calcium oxalate monohydrate (COM) (18). However, the majority of these investigations utilized qualitative metrics for assessing the stone morphology on CT; these metrics were found to be highly subjective and variable, and were not found to be strong predictors of stone fragility.

In this *ex vivo* investigation, we propose to add objective measures of internal morphology to knowledge of stone volume, composition, and surface morphology to predict stone fragility, using metrics derived from routine dose dual-energy CT. Our study aims to do the following: a) identify CT-based metrics describing the internal morphology of kidney stones that correlate with time to comminution, defined as the time required to completely break and remove the stone; and b) assess the predictive ability of using measures obtained from routine dose dual-energy CT protocols to estimate stone fragility.

Materials and Methods

Micro-CT imaging

Stones were scanned with a micro-CT system (SkyScan 1172, Bruker, Belgium) to determine their composition (19). Briefly, each stone was scanned (dry) using 60 kVp with 0.4° rotation steps, averaging 4 images for each step. Final isotropic voxels were 20 μm on a side. Stone compositions were judged using attenuation values and established composition-specific characteristics (20). Stone composition was confirmed by infrared spectroscopy. IRB protocol approval was not required for this non-patient study. However, biospecimen approval was obtained from the institutional biospecimen committee.

Whole-body CT imaging

Subsequent to micro-CT imaging, stones were hydrated for 24 hours in distilled water and embedded in gelatin in a 60-well ice-cube tray. The tray was covered with plastic wrap and inserted into a 35-cm water phantom and scanned with a clinical, state-of-the art, dual-source, dual-energy CT scanner (Somatom Force, Siemens Healthcare, Germany) using the routine stone composition clinical protocol in use at our institution (90/Sn150 kV, 350/219 quality reference mAs, ~8 mGy CTDIvol, 0.5 s rotation time, 192 × 0.6 mm collimation). The data were reconstructed with the same parameters used by our clinical protocol (300 mm field of view (FOV), 1 mm slices, 0.8 mm increment, Br44 reconstruction kernel). The resulting low- and high-energy images were linearly combined to create a set of mixed images. A separate, small FOV (120 mm) reconstruction with smaller pixel size (~0.23 mm) was performed to provide a higher spatial resolution image. A side-by-side comparison of micro-CT and clinical CT images is shown in Figure 1 for a representative stone.

Texture analysis of stone morphology

Each stone in the mixed images was segmented by our in-house stone analysis software (21) using a semi-automated approach to identify the stones and an adaptive threshold method to segment it from the surrounding water. Texture analysis requires the computation of the distribution of co-occurring values at a given offset in the image. Such distribution is often referred to as the co-occurrence matrix and for a 3D image I of size (n,m,o) it is mathematically defined as follows:

$$\mathrm{cooc}_{\Delta x,\Delta y,\Delta z}(i,j)=\sum_{p=1}^{n}\sum_{q=1}^{m}\sum_{r=1}^{o}\begin{cases}1, \text{if } \mathrm{I}(p,q,r)=\mathrm{i} \text{ and } \mathrm{I}(p+\Delta x, q+\Delta y, r+\Delta z)=j\\ 0, \text{otherwise}\end{cases}$$

The offset (Δx,Δy,Δz) depends on the direction used and the distance d at which the matrix is computed. The CT numbers for each stone were discretized in 16 grey levels and 52 different co-occurrence matrices - 13 directions in the 3 dimensions at 4 different pixel distances - were generated from the mixed image for each segmented stone. To calculate the Haralick textural features (22) describing internal morphology, the equations in Table 1 were applied to each co-occurrence matrix and the average computed for each textural feature. Surface roughness (23) and the dual energy CT number ratio (the ratio of the CT number in the low-energy image to that at the same voxel in the high-energy image) (12) were computed as previously described.

Ex-vivo analysis of stone fragility

To measure the fragility of each stone, we attempted to reproduce *ex vivo* the environment of a percutaneous nephrolithotripsy. Each stone was placed in a vial with water and disintegrated using the same ultrasonic lithotripter (Olympus LUS, Melville, NY) used by our surgical urologists. The experimental set-up for the ex-vivo analysis of stone fragility is shown in Figure 2. The same setting of the lithotripter was used for all stones, regardless of their size, as is done in our clinical practice. We recorded the time required to break and completely remove each stone from its vial and used this time to comminution as the figure of merit to quantify stone fragility.

Statistical analysis

Associations between stone morphology characteristics and comminution time were assessed using both simple and multivariable linear regression. Comminution time was evaluated using a natural log transformation for all analyses to account for its skewed distribution. When performing multivariable analyses, models were first adjusted for volume (i.e. two variable models), as this variable was considered *a priori* to be a critical predictor of stone comminution time. Best subset selection methods were used for the remaining predictors, based on the statistical significance of all predictors in the model ($p<0.05$ for all), the variance inflation factors (VIF) of the coefficients to detect the presence of multi-collinearity (VIF<3 for all) and the adjusted R^2 cutoff (24). In order to extend the applicability of the model to single energy CT, we used an identical modeling process to investigate the subset of multivariable models that did not require dual energy. Model size was restricted to three variables due to limited sample size. The best model was then used to predict the comminution time for each stone. All statistical analysis was performed using the R statistical software (25).

Results

Our study cohort consisted of 33 stones: primarily pure calcium oxalate monohydrate (COM) stones (N=7), mixed COM and apatite (APA) stones (N=2), and mixed calcium oxalate (CaOx, which contained both COM and calcium oxalate dihydrate) and APA stones (N=24). The average volume of the stones was 300 mm^3 (range 134–674 mm^3). The average comminution time measured *ex vivo* was 32 s (range 7–115 s). The correlation matrix for the investigated variables is shown in Supplemental Figure 1.

Univariate and volume-adjusted models of stone fragility

We report three kinds of models: univariate (1 variable), volume-adjusted (volume + 1 variable), and best multi-variable model to fit our stone samples (volume + 2 variables). The univariate regression models using a single predictor are shown in Table 2. Despite limitations in spatial resolution associated with clinical CT data, several internal and surface morphological features were found to be significantly associated with time to comminution. In particular, homogeneity, surface roughness and CT number at the higher tube potential selection (HU high) yielded a higher adjusted R^2 than volume.

Table 2 also reports all volume-adjusted models. Three volume-adjusted models met our requirements for statistical significance and acceptable VIF; these models are bolded in Table 2 and are referred to as the best subset. The best volume-adjusted model incorporated CT number ratio because it demonstrated the highest adjusted R-squared ($R^2_{adj} = 0.52$). The next best volume-adjusted model in best subset of models adjusted for volume incorporated max probability ($R^2_{adj} = 0.42$). We note that this model does not include variables that require a dual-energy scan, such as the CT number ratio. Assuming the equivalence of mixed dual-energy CT images to single-energy CT images, this model could be considered representative of single-energy CT scans. It was also noted that the volume-adjusted model using surface roughness had a high R-squared and statistically significant p-value for surface roughness ($p = 0.05$), but the insignificance of volume ($p = 0.53$) and high VIF of 7.3 disqualified this model from our best subset.

Best multivariable “single-energy” CT models of stone fragility

Using the mixed dual-energy images as surrogates for single-energy images, volume, max probability, and sum mean were the best predictors in the multivariable, “single-energy” model (i.e. models without the use of CT number ratio, $R^2_{adj} = 0.54$) (Table 3). The two bolded models (using volume, max probability and surface roughness and volume, max probability and variance) were also included in our best subset. While three other variables (cluster shade, homogeneity, and surface roughness), were statistically significant when individually combined to volume and max probability, the p-value for volume was greater than 0.05 for these models. Additionally, these models had 2 or more VIFs greater than 3.

Best multivariable dual-energy CT models of stone fragility

The best dual-energy CT model included the metrics volume, CT number ratio and peak curvature ($R^2_{adj} = 0.58$), while the best subset additionally included the models using metrics HU Low and HU High, as shown in Table 4.

Discussion

The best multivariable model for a mixed images, which did not take into account energy-specific information, included the metrics stone volume, max probability and sum mean, and accounted for 54% of the variability in stone comminution time (Table 3). The best multivariable model using dual energy metrics included the variables volume, dual-energy CT number ratio and surface roughness, and explained 58% of the variability in comminution time (Table 4). The limited additional contribution of dual-energy metrics is

likely due to the similar mineral composition of the stones in our population, which was intentional in our study design as the vast majority of stones that are removed through PCNL consist of CaOx with different degrees of apatite. Acknowledging the potential importance of stone composition, we used a combination of infrared spectroscopy and microCT to have the best confidence on the minerals contained in our stone specimens (26).

From the scatter plot of the predicted comminution time shown in Figure 3, we see that the distribution of the errors is not even, with 2 of the specimens in particular appearing to be outlying values. This could be due to the fact that important predictor variables have a non-linear relationship with comminution time or have been omitted from the model; however, due to the limited sample size for this study, we are unable to reliably fit more complex models to our data at present.

To our knowledge, our study is the first attempt at introducing quantitative metrics describing stone morphology to predict stone fragility. If validated in vivo, the predictive models for stone fragility developed in this study would provide valuable information for both the urologic surgeon and the patient to better evaluate treatment options. For example, larger, more fragile stones may be amenable to ureteroscopic stone removal or SWL, which are both less invasive procedures; however, smaller, denser stones may be more efficiently and completely cleared with PCNL, justifying this more invasive procedure. This additional information would be available to the urologist without additional radiation dose to the patient, and could be made readily available, as the computational burden to generate the texture features is minimal, taking only a few seconds on a regular computer. There are additional clinical implications of a quantitative fragility model. Larger stone size - which is accounted for in all of our models – increases the rate of complications during PCNL (27). Furthermore, the duration of surgical removal of kidney stones has been shown to be a significant risk factor for the development of postoperative fever (28).

This study has several limitations. The cohort of stones was fairly small and consisted mostly of calcium oxalate stones mixed with different degrees of apatite. As mentioned earlier, this selection of stone types was intentional in this proof of feasibility study, since we did not want differences in stone composition creating additional noise in the data. Several studies in the literature have showed how calcium oxalate is the most prevalent mineral in kidney stones treated clinically by PCNL, with 60–70% of all stones treated consisting predominantly of CaOx (29, 30). Since dual-energy metrics mainly reflect differences in mineral composition, it is not surprising that they provided little additional predictive ability in the fragility models developed from our relatively homogeneous stone population. In future studies, our cohort will be expanded to include stones of different minerals compositions and the fragility models derived from dual energy data are expected to more significantly outperform the ones derived from single energy CT. Moreover, the *ex vivo* analysis of stone fragility precluded inclusion of factors such as the location of the stone in the patient, which can have a major effect on both comminution time and overall surgery outcome. Finally, several of the stones that were analyzed were extracted from the same patients. However, since our fragility models did not make use of any patient-specific characteristics (e.g. urine analysis), we believe that the origin of the stone does not appreciably affect the results.

Conclusions

These preliminary results provide evidence that the routine single and dual energy scan renal stone protocols used in our clinical practice can also provide morphology metrics that can help serve as predictors of stone comminution time. A combination of volumetric, morphological and dual energy characteristics was shown to predict the comminution time with reasonable accuracy (adjusted R^2 = 58%). Without the dual energy metrics, the best model accounted for 54% of the variability in stone comminution time. Currently, a larger study with different stone minerals is ongoing, with the goal of developing a comprehensive model of stone fragility that uses *in vivo* information of stone size composition and morphology to accurately predict its fragility during clinical PCNL.

Supplementary Material

Refer to Web version on PubMed Central for supplementary material.

Acknowledgments

The project described was supported by Grant numbers DK100227, DK083007, and DK101405 from the National Institutes of Health. The content is solely the responsibility of the authors and does not necessarily represent the official views of the National Institutes of Health. The authors would like to acknowledge Kristin Mara for support with the statistical analysis, Amy Krambeck, MD, for arranging the use of the ultrasonic lithotripter for this study and Kris Nunez for assistance in editing the manuscript.

References

1. Pearle MS, Calhoun EA, Curhan GC. Urologic diseases in America project: urolithiasis. J Urol. 2005; 173(3):848–857. [PubMed: 15711292]
2. Litwin, M.; Saigal, C. Economic impact of urologic disease. In: Urologic Diseases in America. Litwin, MS.; Saigal, CS., editors. US Department of Health and Human Services, Public Health Service, National Institutes of Health, National Institute of Diabetes and Digestive and Kidney Diseases. Washington, DC: US Government Printing Office; 2012. p. 494
3. Stamatelou KK, Francis ME, Jones CA, Nyberg LM, Curhan GC. Time trends in reported prevalence of kidney stones in the United States: 1976–1994. Kidney Int. 2003; 63(5):1817–1823. [PubMed: 12675858]
4. Brikowski TH, Lotan Y, Pearle MS. Climate-related increase in the prevalence of urolithiasis in the United States. Proc Natl Acad Sci U S A. 2008; 105(28):9841–9846. [PubMed: 18626008]
5. Auge BK, Preminger GM. Surgical management of urolithiasis. Endocrinol Metab Clin North Am. 2002; 31(4):1065–1082. [PubMed: 12474646]
6. Lingeman J, Newmark J, Wong M. Classification and management of staghorn calculi. Controversies in endourology Philadelphia: Saunders. 1995:136–144.
7. Williams JC Jr, Saw KC, Paterson RF, Hatt EK, McAteer JA, Lingeman JE. Variability of renal stone fragility in shock wave lithotripsy. Urology. 2003; 61(6):1092–1096. discussion 7. [PubMed: 12809867]
8. Coursey CA, Casalino DD, Remer EM, et al. ACR Appropriateness Criteria® acute onset flank pain-suspicion of stone disease. Ultrasound quarterly. 2012; 28(3):227–233. [PubMed: 22902840]
9. Fulgham PF, Assimos DG, Pearle MS, Preminger GM. Clinical effectiveness protocols for imaging in the management of ureteral calculous disease: AUA technology assessment. J Urol. 2013; 189(4): 1203–1213. [PubMed: 23085059]
10. Vrtiska TJ, Takahashi N, Fletcher JG, Hartman RP, Yu L, Kawashima A. Genitourinary applications of dual-energy CT. AJR Am J Roentgenol. 2010; 194(6):1434–1442. [PubMed: 20489081]

11. Stolzmann P, Kozomara M, Chuck N, et al. In vivo identification of uric acid stones with dual-energy CT: diagnostic performance evaluation in patients. Abdom Imaging. 2010; 35(5):629–635. [PubMed: 19727931]
12. Primak AN, Fletcher JG, Vrtiska TJ, et al. Noninvasive differentiation of uric acid versus non-uric acid kidney stones using dual-energy CT. Acad Radiol. 2007; 14(12):1441–1447. [PubMed: 18035274]
13. Yu L, Liu X, Leng S, et al. Radiation dose reduction in computed tomography: techniques and future perspective. Imaging Med. 2009; 1(1):65–84. [PubMed: 22308169]
14. Boll DT, Patil NA, Paulson EK, et al. Renal stone assessment with dual-energy multidetector CT and advanced postprocessing techniques: improved characterization of renal stone composition--pilot study. Radiology. 2009; 250(3):813–820. [PubMed: 19244048]
15. Qu M, Ramirez-Giraldo JC, Leng S, et al. Dual-energy dual-source CT with additional spectral filtration can improve the differentiation of non-uric acid renal stones: an ex vivo phantom study. AJR Am J Roentgenol. 2011; 196(6):1279–1287. [PubMed: 21606290]
16. Williams JC Jr, Hameed T, Jackson ME, et al. Fragility of brushite stones in shock wave lithotripsy: absence of correlation with computerized tomography visible structure. J Urol. 2012; 188(3):996–1001. [PubMed: 22819106]
17. Kim SC, Burns EK, Lingeman JE, Paterson RF, McAteer JA, Williams JC Jr. Cystine calculi: correlation of CT-visible structure, CT number, and stone morphology with fragmentation by shock wave lithotripsy. Urol Res. 2007; 35(6):319–324. [PubMed: 17965956]
18. Zarse CA, Hameed TA, Jackson ME, et al. CT visible internal stone structure, but not Hounsfield unit value, of calcium oxalate monohydrate (COM) calculi predicts lithotripsy fragility in vitro. Urol Res. 2007; 35(4):201–206. [PubMed: 17565491]
19. Zarse CA, McAteer JA, Sommer AJ, et al. Nondestructive analysis of urinary calculi using micro computed tomography. BMC Urol. 2004; 4(1):15. [PubMed: 15596006]
20. Williams JC Jr, McAteer JA, Evan AP, Lingeman JE. Micro-computed tomography for analysis of urinary calculi. Urol Res. 2010; 38(6):477–484. [PubMed: 20967434]
21. Duan X, Wang J, Qu M, et al. Kidney stone volume estimation from computerized tomography images using a model based method of correcting for the point spread function. J Urol. 2012; 188(3):989–995. [PubMed: 22819107]
22. Haralick RM, Shanmugam K, Dinstein IH. Textural features for image classification. IEEE Transactions on Systems, Man and Cybernetics. 1973; SMC-3(6):610–621.
23. Duan X, Qu M, Wang J, et al. Differentiation of calcium oxalate monohydrate and calcium oxalate dihydrate stones using quantitative morphological information from micro-computerized and clinical computerized tomography. J Urol. 2013; 189(6):2350–2356. [PubMed: 23142201]
24. Weiss, NA.; Weiss, CA. Introductory statistics. 7th. Boston: Addison-Wesley Publishing Company; 2005.
25. R Foundation. [Accessed December 14, 2015] What is R? Introduction to R. Available at: https://www.r-project.org/about.html
26. Krambeck AE, Lingeman JE, McAteer JA, Williams JC Jr. Analysis of mixed stones is prone to error: a study with US laboratories using micro CT for verification of sample content. Urol Res. 2010; 38(6):469–475. [PubMed: 20967439]
27. Michel MS, Trojan L, Rassweiler JJ. Complications in percutaneous nephrolithotomy. Eur Urol. 2007; 51(4):899–906. discussion. [PubMed: 17095141]
28. Dogan HS, Sahin A, Cetinkaya Y, Akdogan B, Ozden E, Kendi S. Antibiotic prophylaxis in percutaneous nephrolithotomy: prospective study in 81 patients. J Endourol. 2002; 16(9):649–653. [PubMed: 12490017]
29. El-Assmy AM, Shokeir AA, El-Nahas AR, et al. Outcome of percutaneous nephrolithotomy: effect of body mass index. Eur Urol. 2007; 52(1):199–205. [PubMed: 17161525]
30. Kang DE, Maloney MM, Haleblian GE, et al. Effect of medical management on recurrent stone formation following percutaneous nephrolithotomy. J Urol. 2007; 177(5):1785–1789. [PubMed: 17437820]

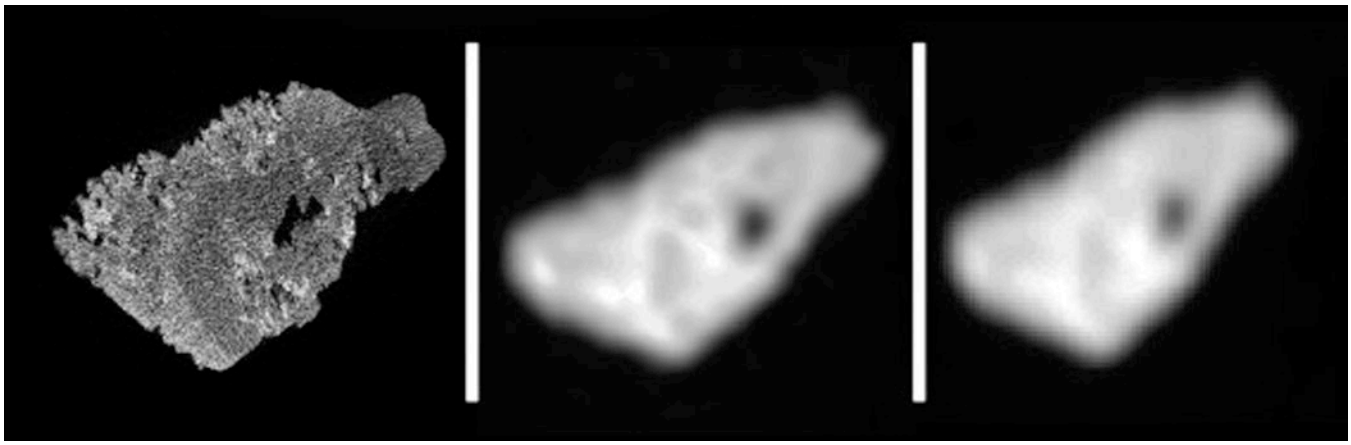

Figure 1.
Qualitative comparison of CT images of a representative stone. Left, reference micro-CT scan used to determine stone composition (CaOx with apatite). Middle: Small field-of-view reconstruction from the routine stone composition protocol at our institution. Right: full field-of-view, clinical CT reconstruction from the same acquired data.

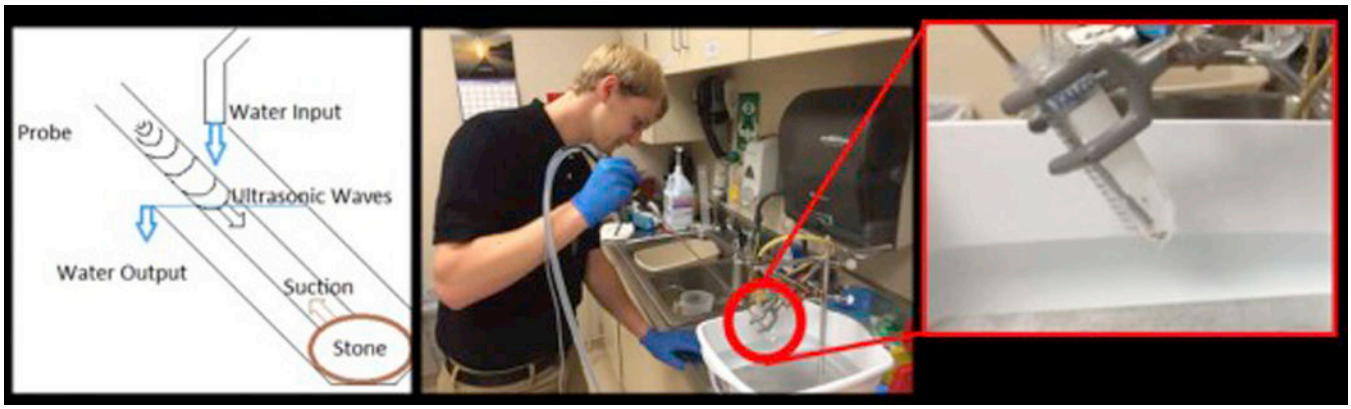

Figure 2.
our ex-vivo experiment to measure time to comminution for each stone

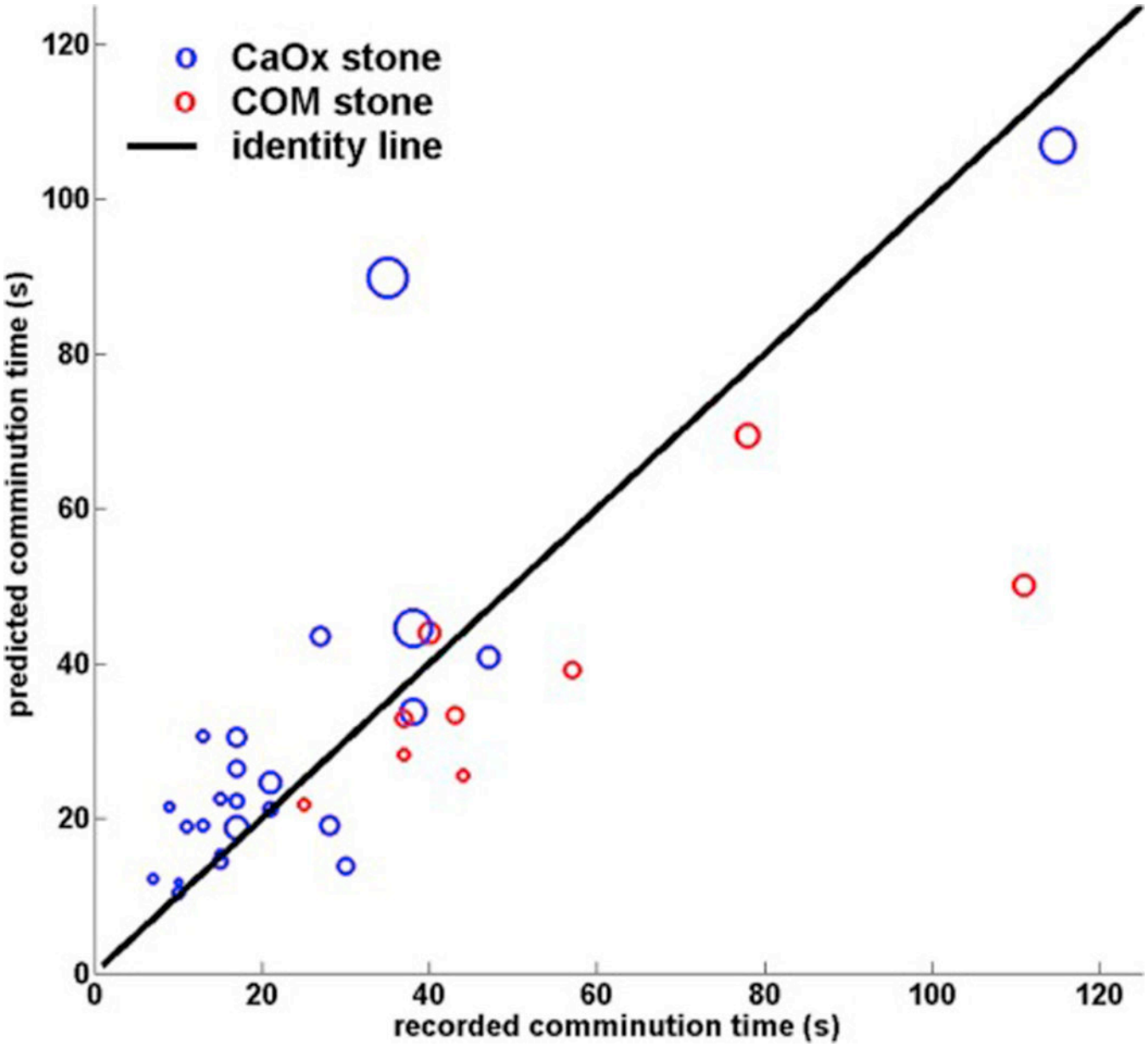

Figure 3.

Plot comparing observed vs predicted comminution time based on the multivariable model with predictors volume, CT ratio and shape index. The size of each point is proportional to that stone's volume (mm^3)

Table 1

Haralick features describing stone internal morphology (1–12) and features describing stone surface (13–15) cooc = co-occurrence matrix [22,23,30].

Variable	Formula	Interpretation
1. Energy	$\sum_{i=1}^{\text{num\_levels}} \sum_{j=1}^{\text{num\_levels}} \text{cooc}(i,j)^2$	Uniformity of the Image
2. Entropy	$\sum_{i=1}^{\text{num\_levels}} \sum_{j=1}^{\text{num\_levels}} \text{cooc}(i,j)\log_{10}(\text{cooc}(i,j))$	Randomness of the image
3. Correlation	$\sum_{i=1}^{\text{num\_levels}} \sum_{j=1}^{\text{num\_levels}} ((i-\mu_x)*(j-\mu_y)*(\text{cooc}(i,j)/(\sigma_x*\sigma_y))$	Local gray level linear dependency of the image
4. Contrast	$\sum_{i=1}^{\text{num\_levels}} \sum_{j=1}^{\text{num\_levels}} \text{cooc}(i,j)*\lvert i-j\rvert^2$	Measure of local variations in the image
5. Homogeneity	$\sum_{i=1}^{\text{num\_levels}} \sum_{j=1}^{\text{num\_levels}} \frac{\text{cooc}(i,j)}{\lvert i-j\rvert+1}$	Local homogeneity of the image
6. Variance	$\sum_{i=1}^{\text{num\_levels}} \sum_{j=1}^{\text{num\_levels}} ((i-\mu_x)^2+(j-\mu_y)^2)*\text{cooc}(i,j)$	Gray-level variability of the pixel pairs
7. Sum Mean	$\sum_{i=1}^{\text{num\_levels}} \sum_{j=1}^{\text{num\_levels}} \text{cooc}(i,j)*(i+j)$	N.A.
8. Inertia	$\sum_{i=1}^{\text{num\_levels}} \sum_{j=1}^{\text{num\_levels}} \text{cooc}(i,j)*(i+j)^2$	N.A.
9. Cluster Shade	$\sum_{i=1}^{\text{num\_levels}} \sum_{j=1}^{\text{num\_levels}} (i+j-\mu_x-\mu_y)^3\text{cooc}(i,j)$	Skewness of the image.
10. Cluster Tendency	$\sum_{i=1}^{\text{num\_levels}} \sum_{j=1}^{\text{num\_levels}} (i+j-\mu_x-\mu_y)^4\text{cooc}(i,j)$	Another measure of asymmetry of the image
11. Max probability	***max*(*cooc*)**	N.A.
12. Inverse variance	$\sum_{i=1}^{\text{num\_levels}} \sum_{j=1}^{\text{num\_levels}} \frac{\text{cooc}(i,j)}{\lvert i-j\rvert^2}$	Local homogeneity of the image
13. Shape Index	FWHM of histogram of vertex curvatures	Overall surface morphology of a stone

Table 2

Association between DECT-derived morphology metrics and comminution time, unadjusted and adjusted for volume

Imaging Variable		Unadjusted Model		Adjusted for Volume			
		P_{var}	R^2	P_{var} [1]	P_{vol} [2]	VIF [3]	R^2_{adj}
Volumetric	**Volume**	**0.0002**	**0.37** *				
	Porosity	0.25	0.04	0.12	0.0001	1.00	0.39
Internal morphology	**Energy**	0.24	0.04	0.09	0.0001	1.7	0.39
	Entropy	0.24	0.04	0.43	0.0003	1.34	0.35
	Correlation	0.34	0.03	0.98	0.0003	1.09	0.33
	Contrast	0.55	0.01	0.85	0.0002	1.05	0.33
	Homogeneity	**<0.0001**	**0.42**	0.12	0.60	5.12	0.38
	Variance	0.84	0	0.27	0.0001	1.10	0.36
	Sum Mean	0.005	0.23	0.50	0.01	1.78	0.34
	Inertia	0.55	0.01	0.85	0.0002	1.05	0.33
	Cluster Shade	0.0002	0.36	0.23	0.15	2.98	0.37
	Clusters Tendency	0.15	0.07	0.37	0.0004	1.05	0.35
	Max Probability	0.37	0.03	**0.04**	**<0.0001**	**1.66**	**0.42** **
	Inverse Variance	0.047	0.12	0.14	0.0005	1.06	0.38
Surface morphology	**Shape Index**	0.27	0.04	0.11	0.0001	1.00	0.39
	Peak Curvature	0.52	0.01	0.45	0.0002	1.00	0.35
	Mean Curvature	**<0.0001**	**0.48**	0.02	0.53	7.30	0.45
DECT	**CT Number Ratio**	0.25	0.04	**0.002**	**<0.0001**	**1.11**	**0.52** ***
	HU Low (90 kVp)	0.004	0.23	0.45	0.01	1.75	0.35
	HU High (150 kVp)	**0.0001**	**0.38**	**0.02**	**0.03**	**1.52**	**0.44**

[1] p-value testing: $\beta_1 = 0$ in the model: log(Comminution time) = $\beta_0 + \beta_1$*variable + β_2*volume

[2] p-value testing: $\beta_2 = 0$ in the model: log(Comminution time) = $\beta_0 + \beta_1$*variable + β_2*volume

[3] Magnitude of the inflation in s.e.(β_1) and s.e.(β_2) due to co-linearity

* Best unadjusted model

** Best single energy model adjusted for volume

*** Best dual energy model adjusted for volume

Acad Radiol. Author manuscript; available in PMC 2017 December 01.

Table 3

Multi-variable, single energy models

Imaging Variable		Adjusted for Volume and Max Probability						
		P_{var} *1*	P_{vol} *2*	$P_{MaxProb}$ *3*	VIF_{var} *4*	VIF_{vol} *5*	$VIF_{MaxProb}$ *6*	R^2_{adj}
volumetric	**Volume**							
	Porosity	0.15	<0.0001	0.052	1.01	1.67	1.68	0.44
internal morphology	**Energy**	0.65	0.0001	0.21	10.4	1.72	10.2	0.41
	Entropy	0.59	<0.0001	0.051	2.07	1.68	2.58	0.41
	Correlation	0.38	<0.0001	0.03	1.26	2.08	1.93	0.42
	Contrast	0.23	<0.0001	0.02	1.27	2.05	2.02	0.43
	Homogeneity	0.0002	0.95	0.0001	7.36	5.25	2.39	0.63
	Variance	**0.01**	**<0.0001**	**0.002**	**1.40**	**2.29**	**2.11**	**0.52**
	Sum Mean	**0.006**	**0.0003**	**0.0008**	**2.91**	**1.89**	**2.72**	**0.54** *
	Inertia	0.23	<0.0001	0.02	1.27	2.05	2.02	0.43
	Cluster Shade	<0.0001	0.13	<0.0001	5.43	3.01	3.03	0.68
	Clusters Tendency	0.12	<0.0001	0.02	1.12	1.66	1.77	0.45
	Max Probability							
	Inverse Variance	1.00	0.002	0.16	2.27	3.16	3.56	0.40
surface morphology	**Shape Index**	**0.02**	**<0.0001**	**0.008**	**1.06**	**1.73**	**1.76**	**0.50**
	Peak Curvature	0.63	<0.0001	0.051	1.02	1.68	1.70	0.41
	Mean Curvature	0.003	0.81	0.006	7.49	7.49	1.71	0.57

1 p-value testing: $\beta_1 = 0$

2 p-value testing: $\beta_2 = 0$

3 p-value testing $\beta_3 = 0$

4 Magnitude of the inflation in s.e.(β_1) due to volume and max probability being in the model

[5] Magnitude of the inflation in s.e.(β2) due to the variable and max probability being in the model

[6] Magnitude of the inflation in s.e.(β3) due to volume and the variable being in the model

* Best single energy model with 3 predictors

Table 4

Multi-variable, dual energy models

Imaging Variable		Adjusted for Volume and CT Ratio						
		P_{var} *1*	P_{vol} *2*	P_{CTR} *3*	VIF_{var} *4*	VIF_{vol} *5*	VIF_{CTR} *6*	R^2_{adj}
Volumetric	**Volume**							
	Porosity	0.13	<0.0001	0.002	1.01	1.11	1.12	0.54
Internal morphology	**Energy**	0.78	<0.0001	0.009	2.26	1.71	1.47	0.51
	Entropy	0.90	<0.0001	0.003	1.41	1.38	1.18	0.51
	Correlation	0.92	<0.0001	0.002	1.09	1.2	1.12	0.51
	Contrast	0.84	<0.0001	0.002	1.05	1.16	1.11	0.51
	Homogeneity	0.03	0.40	0.0005	5.18	5.13	1.13	0.59
	Variance	0.21	<0.0001	0.002	1.1	1.22	1.11	0.53
	Sum Mean	0.24	0.0006	0.001	1.8	1.84	1.13	0.53
	Inertia	0.84	<0.0001	0.002	1.05	1.16	1.11	0.51
	Cluster Shade	0.03	0.057	0.0003	3.11	2.98	1.16	0.59
	Clusters Tendency	0.20	<0.0001	0.001	1.05	1.15	1.12	0.53
	Max Probability	0.70	<0.0001	0.02	2.57	1.7	1.72	0.51
	Inverse Variance	0.87	<0.0001	0.006	1.34	1.31	1.41	0.51
Surface morphology	**Shape Index**	**0.03**	**<0.0001**	**0.0006**	**1.01**	**1.12**	**1.12**	**0.58** *
	Peak Curvature	0.56	<0.0001	0.002	1.01	1.12	1.12	0.51
	Mean Curvature	0.03	0.84	0.003	7.53	7.91	1.15	0.58
DECT	**CT Number Ratio**							
	HU Low (90 kVp)	**0.04**	**0.001**	**0.0003**	**1.92**	**1.76**	**1.22**	**0.57**
	HU High (150 kVp)	**0.04**	**0.001**	**0.003**	**1.57**	**1.74**	**1.15**	**0.57**

[1] p-value testing: $\beta_1 = 0$

[2] p-value testing: $\beta_2 = 0$

[3] p-value testing $\beta_3 = 0$

[4] Magnitude of the inflation in s.e.(β 1) due to volume and CT Ratio being in the model

[5] Magnitude of the inflation in s.e.(β_2) due to the variable and CT Ratio being in the model

[6] Magnitude of the inflation in s.e.(β_3) due to volume and the variable being in the model

* Best dual energy model with 3 predictors